Wireless Vehicular Multiband Measurements in Centimeterwave and Millimeterwave Bands

Markus Hofer*, David Löschenbrand*, Jiri Blumenstein†, Herbert Groll◇, Stefan Zelenbaba*, Benjamin Rainer*, Laura Bernadó*, Josef Vychodil†, Tomas Mikulasek†, Erich Zöchmann‡, Seun Sangodoyin∐, Hussein Hammoud∐, Bernhard Schrenk*, Robert Langwieser◇, Stefan Pratschner◇,⊕, Ales Prokes†, Andreas F. Molisch∐, Christoph F. Mecklenbräuker◇, and Thomas Zemen*

*Security & Communication Technologies, AIT Austrian Institute of Technology GmbH, Austria
† Dept. of Radio Electronics, Brno University of Technology, Czech Republic
⊕ Christian Doppler Laboratory for Dependable Wireless Connectivity for the Society in Motion, Austria
◇Institute of Telecommunications, TU Wien, Austria
‡Propagation Ideas & Solutions GmbH, Austria
∐Wireless Devices and Systems Group, University of Southern California, USA
Email: markus.hofer@ait.ac.at

***Abstract*—In this paper we present a software defined radio (SDR) based measurement framework that allows for simultaneous measurements of wireless communication channels over multiple bands. We present and discuss results of a wireless vehicular-to-infrastructure multiband channel measurement campaign at center frequencies of 3.2 GHz, 34.3 GHz and 62.35 GHz in a street crossing scenario. The measurement is conducted using a bandwidth of 155.5 MHz and a sounding repetition rate of 31.25 μs. We compare the measurements using the time-variant power delay profile (PDP) and the Doppler spectral density (DSD).**

***Index Terms*—multiband, mmWave, wireless channel measurements, wireless channel sounding, software defined radio**

I. Introduction

According to the Cisco visual network index, mobile data traffic will grow to 900 exabytes annually by 2022, compared to 138 exabytes in 2017 [1]. The current sub-6 GHz frequency bands are heavily utilized, hence, exploiting millimeter wave (mmWave) bands is of highest importance. Typically used for fixed wireless and small-cell applications, their utilization for vehicle-to-everything (V2X) or machine-to-machine (M2M) communication with high reliability and ultra-low latency requirements, demand a dedicated research effort. Understanding channel properties at these higher frequencies in different scenarios is key for designing protocols, algorithms and hardware that are able to fulfill these ambitious goals.

While sub-6 GHz bands provide less bandwidth, propagation conditions are more advantageous, in particular showing a lower isotropic free-space pathloss, and smaller sensitivity to blockage. Consequently, a comparison of the propagation in sub-6 GHz bands versus the mmWave bands is important for system design, also in light of possible multiband transmission where, e.g., basic information is transmitted in a low-frequency band, while additional data is transmitted in the mmWave links when they are available; this principle is well known from non-standalone fifth generation (5G) systems [2]. Finally, the information in one frequency band can be used to help channel estimation and beam forming in the other band [3], [4].

Recent multiband measurements for static scenarios are presented in [5]–[7]. In [5] the authors investigate a static vehicle-to-vehicle (V2V) multiband measurement at frequency bands 6.75 GHz, 30 GHz and 60 GHz for a "T"-intersection. The results show that significant scatterers are visible in all frequency bands. Multiband measurements at 6.75 GHz, 30 GHz, 60 GHz and 73 GHz for a static V2V scenario under the presence of vehicular blocking are presented in [6]. The authors analyze the blockage loss of small blockers (vehicles) and of large blockers (buses). Similar to [5], they found that significant specular reflections in the 6.75 GHz bands occur in both mmWave bands at 30 GHz and 60 GHz. The authors of [7] presented simultaneous double-directional ultra-wideband multiband measurements at 6.75 GHz, 33.75 GHz and 60.75 GHz in street canyon scenarios. An analysis of the aspects of scattering and large scale parameters in the different bands is discussed.

Recent results of single band vehicle-to-infrastructure (V2I) mmWave measurements are presented in [8]–[10]. In [8], V2I channel measurements at 28 GHz for 500 MHz bandwidth for an expressway scenario are shown and multipath components caused by static and moving objects like vehicles on the expressway are identified. In [9], V2I channel measurements at 60 GHz with a bandwidth of 8 GHz are presented. The scenario considers an overhead installation and evaluates the power delay profile and the root mean square delay spread. In [10], V2I channel measurements at 60 GHz with horn antennas at different elevation angles are performed and different antenna switching strategies are investigated.

Scientific contribution:

- We present a software defined radio (SDR) based channel

sounder for simultaneous channel measurements in three different frequency bands.
- In contrast to the already shown static multiband measurement we show first results for a V2I multiband measurement for a street crossing scenario with moving transmitter (TX) at center frequencies of 3.2 GHz, 34.3 GHz and 62.35 GHz.

II. Measurement Setup

We perform channel sounding measurements simultaneously at 3.2 GHz, 34.3 GHz and 62.35 GHz to obtain the time-variant channel transfer function $H_i[m, q]$, where i indicates the frequency band. The time index is denoted by $m \in \{0, \ldots, M-1\}$ and the frequency index by q. We use a multitone channel sounding approach for the measurements (see Sec. II-C for more details on the sounding signal). In order to make the results comparable across frequency bands, we use antennas with comparable patterns. Namely a donut-shaped omni-directional pattern at the TX and a directional pattern at the receiver (RX). Vertically polarized antennas are used for the measurement. The details of the antennas at the TX and RX side and their positioning are given in Sec. II-A and Sec. II-B, respectively.

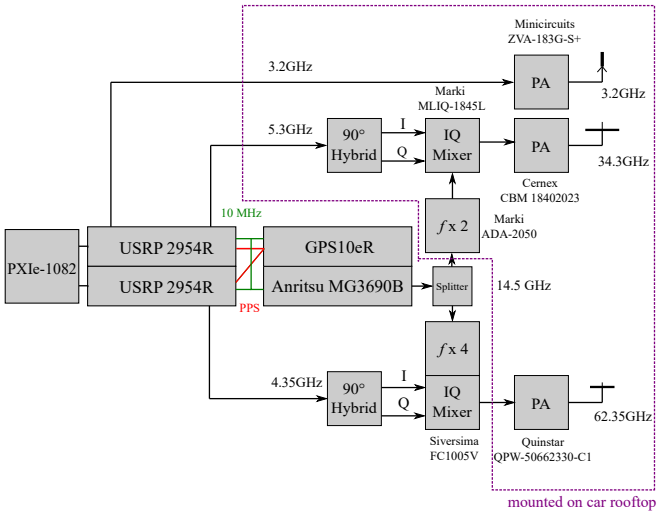

Fig. 1. Schematic diagram of the TX.

A. Transmitter

At the TX, shown in Fig. 1, two National Instruments (NI) universal software radio peripheral (USRP) 2954R [11] SDRs generate multitone based sounding signals with a bandwidth of 155.5 MHz at center frequencies 3.2 GHz, 4.35 GHz and 5.3 GHz, respectively. The USRPs are controlled by an NI PXIe-1082. Synchronization and triggering is performed via a Rubidium clock. The 10 MHz and pulse per second (PPS) signals are distributed to the two USRPs simultaneously for synchronization.

The 3.2 GHz sounding signal is amplified by a Minicircuits ZVA-183G-S+ power amplifier (PA). The 5.3 GHz and 4.35 GHz intermediate frequency (IF) signals are up-converted using separate radio frequency (RF) up-conversion stages, where the IF signals are mixed with a local oscillator (LO) to obtain 34.3 GHz and 62.35 GHz, respectively. Each up-conversion stage uses 90°-hybrid couplers to convert the IF signal to I/Q signals. The LO signal is generated at $f_{\text{LO-TX}} = 14.5$ GHz by an Anritsu MG3690B signal generator whose 10 MHz reference signal is obtained from the Rubidium clock. Using a splitter, the LO signal is fed to both conversion stages. For the 34.3 GHz stage the LO signal is doubled in frequency by a Marki ADA-2050 doubler. A Marki MLIQ-1845L mixes the 29 GHz LO signal with the 5.3 GHz I/Q input signal to obtain the RF signal at 34.3 GHz. A Cernex CBM18402023 is used for amplification. The up-conversion stage for 62.35 GHz uses a Siversima FC1005V that consists of a frequency quadrupler and I/Q mixer integrated in one device. The Siversima is modified to allow for an external LO input. The LO signal is quadrupled to 59 GHz and mixed with the 4.35 GHz IF I/Q signal to obtain the RF signal at 62.35 GHz. As amplifier a Quinstar QPW-50662330-C1 is utilized.

Custom-built omni-directional monopole antennas are utilized as TX antennas. For 34.3 GHz and 62.35 GHz, $\lambda/4$ monopole antennas with metallic ground planes are used. The shape of the ground plane is rectangular for 34.3 GHz and circular for 62.35 GHz. The ground plane size is about 14 λ in the 34.3 GHz band and about 12 λ in the 62.35 GHz band. At 3.2 GHz a $\lambda/4$ monopole antenna with radials is used to attain a comparable pattern at reduced size.

The equipment is fixed on a breadboard with size $60 \times 60\,\text{cm}^2$. It is a solid aluminum breadboard with a grid of through-tapped mounting holes. The breadboard is mounted on luggage racks on the cars' rooftop as shown in Fig. 2. Optical posts are used to fix the 34.3 GHz and 62.35 GHz transmit antennas. The antenna heights are chosen such that the ground planes are on the same height. The antennas are mounted in a straight line towards driving direction with the 62.35 GHz antenna in the front, followed by the 34.3 GHz and the 3.2 GHz antenna.

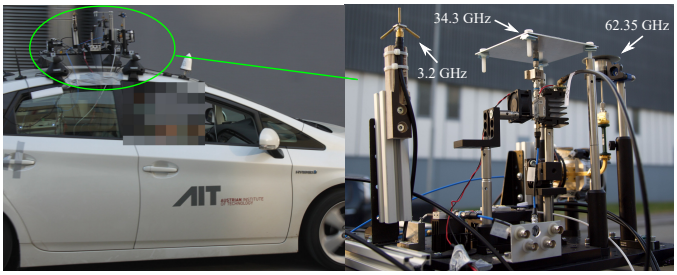

Fig. 2. Transmit antennas mounted on car rooftop.

B. Receiver

The RX, shown in Fig. 3, is built similarly to the TX. Three USRPs record the received sounding signals at the three frequency bands simultaneously. The USRPs are controlled by an NI PXIe-1085 equipped with a RAID hard disk that stores

the measurement data. Synchronization is done via a Rubidium clock. The 10 MHz and PPS signals are distributed via a clock distribution device to all three USRPs simultaneously for synchronization.

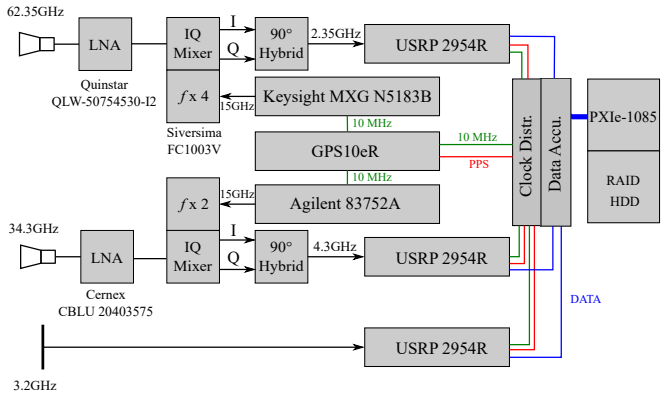

Fig. 3. Schematic diagram of the RX. Note that the IF frequencies are chosen differently at the RX to avoid IF crosstalk.

For 3.2 GHz, the receive antenna is connected to the USRP RF input via a cable. For 34.3 GHz and 62.35 GHz, low noise amplifiers (LNAs) with down-conversion stages are utilized. The 34.3 GHz down-conversion stage consists of the same components as the up-conversion stage. We use a Cernex CBLU 20403575 as LNA. A bandpass filter, not shown in the figure, filters the output signal of the LNA. Due to limited output power of the available signal generators, two separate signal generators are used to generate the LO signal at $f_{\text{RX-LO}} = 15\,\text{GHz}$. For the 34.3 GHz stage the LO signal is generated by an Agilent 83752A signal synthesizer. The LO signal is doubled in frequency and mixed with the 34.3 GHz RF signal to obtain the IF signal at 4.3 GHz which is received by the USRP. The 62.35 GHz down-conversion stage uses a Quinstar QLW-50754530-I2 LNA, which is followed by a Siversima FC1003V mixer with quadrupled LO input. For LO generation we use a Keysight MXG N5183B. The LO signal is quadrupled in frequency and mixed with the 62.35 GHz RF signal to obtain the IF signal at 2.35 GHz which is provided to the USRP RF input via cable.

The directional RX antennas are mounted on a tripod as shown in Fig. 4. For 3.2 GHz a patch array antenna with 17° half power beam width (HPBW) and 18 dBi gain is used, for 34.3 GHz a Fairview SMH128KR-20 standard gain horn antenna with 18.3° HPBW and 20 dBi gain is utilized and for 62.35 GHz a Pasternack PE-9881-20 conical horn antenna with 18° HPBW and 20 dBi gain is utilized. The center of the 3.2 GHz patch antenna is mounted 159 cm above ground level. The distance between 3.2 GHz patch and 34.2 GHz horn antenna is 34.8 cm and 64 cm between patch and conical horn antenna. We permanently monitor the received signal's spectrum to detect possible interference signals.

C. Sounding Signal

A complex baseband multitone signal (orthogonal frequency division multiple access (OFDM) based) is used to capture

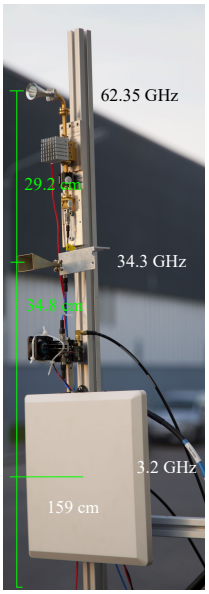

Fig. 4. Receive antennas mounted on a pole of a tripod.

the channel characteristics [12], [13]. The multitone signal consists of $Q = 311$ subcarriers. We choose the subcarrier spacing of $\Delta f = 1/T = 500\,\text{kHz}$, with T the period of the sounding signal, such that we achieve a maximum excess delay of $\tau_{\text{max}} = 2\,\mu\text{s}$. Hence, the effective sounding bandwidth is $B = Q\Delta f = 155.5\,\text{MHz}$.

We use the method of [14] to obtain a multitone signal with a crest factor of 1.25 (see [12] for more details). The sounding signal is constructed by concatenating five repetitions of the multitone signal as shown in Fig. 5. This leads to a total sounding signal length of $5T = 10\,\mu\text{s}$. We use the first period T of the sounding signal as cyclic prefix (CP).

At the RX, the sounding signal is sampled and stored. Due to CP OFDM resemblance of the sounding signal, the frequency domain signal at the RX is directly obtained by a discrete fast Fourier transform (FFT). Two repetitions of the multitone signal are used to obtain an oversampled frequency domain signal. Since the sounding signal is known at the RX, the calibrated channel transfer function is obtained by dividing the received sounding signal by the known sounding signal for every second subcarrier, i.e., [12]

$$\hat{H}[q] = \frac{Y[q]}{X[q]\hat{H}^{\text{RF}}[q]}, \tag{1}$$

where $\hat{H}^{\text{RF}}[q]$ is the calibration transfer function of the RF chains, q is the subcarrier index, $X[q]$ are the known complex weights of the sounding signal at the different subcarriers and $Y[q]$ are the complex weights of the subcarriers after downsampling. The calibration function is obtained by connecting TX with RX directly via attenuators and measuring the transfer function. For better signal-to-noise ratio (SNR) of the calibration transfer function it is averaged over 64 repetitions.

For each frequency band the same principle is used. The longest recorded measurement time is 30 s. The time in-

terval between sounding signals is $T_{\mathrm{R}} = 31.25\,\mu\mathrm{s}$. Using $f_{\mathrm{Dmax}} = 1/(2T_{\mathrm{R}})$ this allows Doppler estimation up to a relative velocity of $v_{\max} = c_0 f_{\mathrm{Dmax}}/f_{\mathrm{c}} = c_0/2T_{\mathrm{R}}f_{\mathrm{c}}$=76.93 m/s, where c_0 is the speed of light and f_{c} is the carrier frequency of the highest frequency band.

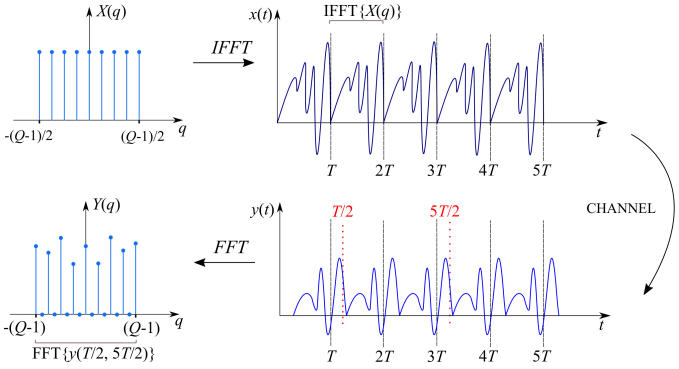

Fig. 5. Sounding Signal structure.

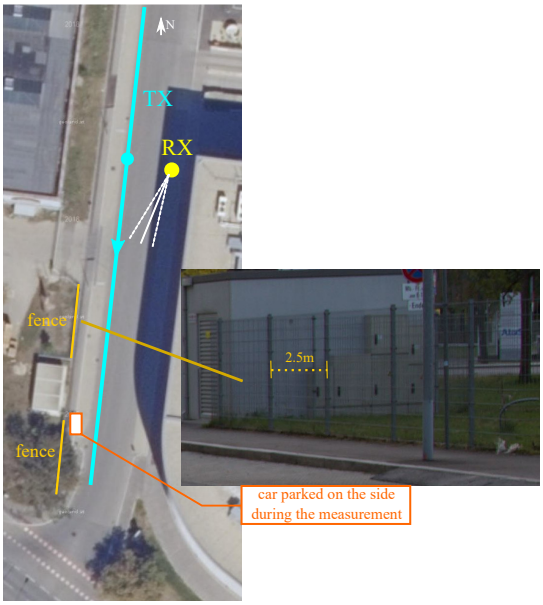

Fig. 6. Overview of scenario [15]. A car approaches a "T"-intersection and stops. The directive horn antennas are pointed towards the road intersection. On the right side of the road there is a metallic fence with metallic pillars.

D. Synchronization

At TX and RX, Precision Test Systems GPS10eR Rubidium clocks provide a 10 MHz reference signal with low phase noise and a PPS signal for timing synchronization between TX and RX. Before the measurement starts, the RX Rubidium clock is connected via coaxial cables to the TX Rubidium clock and disciplined. The TX Rubidium clock acts as primary clock source. After synchronization of about one hour and after a calibration measurement, the Rubidium clocks are separated and both clocks are set to free-run mode [12].

III. Scenario Description

We conduct channel measurements for a V2I scenario in an industrial area in Vienna. The TX car passes the RX that is placed on the left side of the street, approaches a "T"-intersection with traffic lights and stops. The RX antennas are pointed towards the stop point at the road intersection. During the measurement a car parked directly at the road intersection (see Fig.6)

IV. Measurement Evaluation

A. Local Scattering Function

For measurement evaluation the local scattering function (LSF) is utilized. With the time-variant frequency transfer function $H[m,q]$ the estimate of the LSF is given as

$$\hat{\mathcal{C}}[k_{\mathrm{t}};n,p] = \frac{1}{IJ}\sum_{w=0}^{IJ-1}\left|\mathcal{H}^{(G_w)}[k_{\mathrm{t}};n,p]\right|^2. \tag{2}$$

with the Doppler index $p \in \{-M/2\ldots, M/2-1\}$ and the delay index $n \in \{0,\ldots,Q-1\}$. The delay and Doppler shift resolution are defined by $\tau_{\mathrm{s}} = 1/Q\Delta f$ and $\nu_{\mathrm{s}} = 1/MT_{\mathrm{R}}$. The windowed frequency response is

$$\mathcal{H}^{(G_w)}[k_{\mathrm{t}};n,p] = \sum_{m=-M/2}^{M/2-1}\sum_{q=-Q/2}^{Q/2} H[m+Mk_{\mathrm{t}},q] \cdot G_w[m,q]\mathrm{e}^{-\mathrm{j}2\pi(pm-nq)}, \tag{3}$$

where the tapers $G_w[m,q]$ are two-dimensional discrete prolate spheroidal (DPS) sequences as shown in detail in [16], [17]. The number of tapers in the time and frequency domain is set to $I=2$ and $J=1$, respectively [16], [18].

For a first analysis of the measurement results we choose $M = 3200$, which corresponds to an observation duration of 100 ms. For a velocity of $v = 10$ m/s (see velocity in presented figures), this corresponds to a calculation of the LSF over a spatial window of approximately $10.67\,\lambda_1$ for 3.2 GHz, $114.33\,\lambda_2$ for 34.3 GHz and $207.33\,\lambda_3$ for 62.35 GHz, with $\lambda_i, i \in \{1,\ldots,3\}$ being the wavelengths of the different frequency bands. The best choice of the stationarity region length is under investigation.

We calculate the power delay profile (PDP) and Doppler spectral density (DSD) as the expectation of the LSF over the Doppler domain or the delay domain, respectively:

$$\hat{\mathcal{P}}_\tau[k_{\mathrm{t}};n] = E_p\left\{\hat{\mathcal{C}}[k_{\mathrm{t}};n,p]\right\} = \frac{1}{M}\sum_{p=-M/2}^{M/2-1}\hat{\mathcal{C}}[k_{\mathrm{t}};n,p], \tag{4}$$

$$\hat{\mathcal{P}}_\nu[k_{\mathrm{t}};p] = E_n\left\{\hat{\mathcal{C}}[k_{\mathrm{t}};n,p]\right\} = \frac{1}{Q}\sum_{n=0}^{Q-1}\hat{\mathcal{C}}[k_{\mathrm{t}};n,p]. \tag{5}$$

To allow for a better comparability between different frequency bands we normalize the Doppler shifts of the DSDs

to their respective wavelength obtaining normalized Doppler shifts or velocities

$$v_i = f_{\mathrm{D},i}\lambda_i, \tag{6}$$

and show the normalized DSDs over time in the plots discussed in the next section.

B. Analysis of PDPs and DSDs

Furthermore, we normalize the power of the PDPs and DSDs by their respective maxima within their frequency band, i.e., for each frequency band we calculate $\hat{\mathcal{P}}_\tau^{\mathrm{N}}[k_\mathrm{t};n] = \hat{\mathcal{P}}_\tau[k_\mathrm{t};n]/\max_{k_\mathrm{t};n}(\hat{\mathcal{P}}_\tau[k_\mathrm{t};n])$ and $\hat{\mathcal{P}}_\nu^{\mathrm{N}}[k_\mathrm{t};n] = \hat{\mathcal{P}}_\nu[k_\mathrm{t};n]/\max_{k_\mathrm{t};n}(\hat{\mathcal{P}}_\nu[k_\mathrm{t};n])$ We define the dynamic range (DR) as the difference between maximum power and noise floor of each frequency band, where the noise floor is calculated by the median (see [18]). For a fair comparison, we choose the DR to be the smallest one of the three bands. We set values smaller than the DR to be the value of the corresponding noise floor. The plots in Fig. 7-9 show the measurement results of the "T"-intersection scenario, where the car stops at the traffic light. Since the car did not move afterwards we limit the displayed time to 25 s.

In Figures 7(a) - 9(a) we see the time-variant PDPs. We limit the displayed delay to 1 μs, since no significant components were observed for larger delays. Since the directional antennas are pointing towards the road intersection only little energy contribution is observed within the first 10 seconds of the measurement. A comparison of the PDPs reveals similar structures in all three frequency bands. Specifically, e.g., the line-of-sight component is clearly visible.

The normalized time-variant DSDs are shown in Figures 7(b)-9(b). While the TX moves towards the RX the velocity is positive. At 11.6 s the TX passes the RX and the main velocity component becomes negative, since the TX moves away from the RX. For the chosen DR certain scatterers from seconds 9 to 11, caused by e.g., lamp posts and other metallic objects that are visible in the 3.2 GHz band are not visible in the mmWave bands. We consider the increased path loss at mmWave bands as possible reason for that. Furthermore, an increased directionality of reflected components at mmWave frequencies could also lead to the decreased visibility. An interesting structure can be observed within seconds 12 to 17. The plots show distinctive Doppler components at the bands 34.3 GHz and 62.35 GHz. The Doppler components form almost parallel lines and spread from positive to negative Doppler shift. Compared to the 34.3 GHz, the number of lines is higher in the 62.35 GHz band, in the 3.2 GHz the structure is not visible. A first assessment of these results considers a metallic fence with straight metallic pillars located on the right side of the road in driving direction (as indicated in Fig. 6) to be the reason for the distinctive Doppler components. The fence has a regular grid structure with metallic pillars at a distance of around 2.5 m and a height of 2.1 m. The vertical wires of the meshed grid are spaced 5 cm, while horizontal wires are spaced 11 cm apart. It should be noted that the observation window used for evaluating the LSF considers more wavelengths for the evaluation of the LSF at higher center frequencies.

V. Conclusion

In this paper we presented the structure of an SDR based channel sounder that allows for truly simultaneous channel measurements at multiple frequency bands. We showed first results of a V2I multiband measurement campaign at the frequency bands 3.2 GHz, 34.3 GHz and 62.35 GHz for a "T"-intersection with mobile transmitter. By choosing antennas with comparable antenna patterns, i.e., omni-directional antenna patterns at the TX and directional antenna patterns at the RX for the different frequency bands we allow for comparability of the measurement results. The results indicate that the bands show strong similarities in terms of PDP and DSD, however, certain aspects are only visible at higher center frequencies for a fixed observation window length.

Acknowledgment

This work was supported in part by the Austrian Research Promotion Agency FFG through the TRITON project (grant agreement No 858697). This work was funded within the project DEDICATE (Principal Scientist grant) at the AIT Austrian Institute of Technology. The work of H. Hammoud and A. F. Molisch was supported by Caltrans and NSF. This work was supported by the 5G Internet of Things - Doctoral School.

References

[1] Cisco, "VNI Mobile Forecast Highlights," 2019. [Online]. Available: https://www.cisco.com/c/dam/assets/sol/sp/vni/forecast_highlights_mobile/pdf/Global_2022_Forecast_Highlights.pdf

[2] E. Dahlman, S. Parkvall, and J. Skold, *5G NR: The next generation wireless access technology*. Academic Press, 2020.

[3] A. Ali, N. González-Prelcic, and R. W. Heath, "Millimeter wave beam-selection using out-of-band spatial information," *IEEE Transactions on Wireless Communications*, vol. 17, no. 2, pp. 1038–1052, 2017.

[4] D. Burghal, R. Wang, and A. F. Molisch, "Band assignment in dual band systems: A learning-based approach," in *MILCOM 2018-2018 IEEE Military Communications Conference (MILCOM)*. IEEE, 2018, pp. 7–13.

[5] D. Dupleich, R. Muller, C. Schneider, S. Skoblikov, J. Luo, M. Boban, G. Del Galdo, and R. Thoma, "Multi-band vehicle to vehicle channel measurements from 6 GHz to 60 GHz at "T" intersection," in *2019 IEEE 2nd Connected and Automated Vehicles Symposium (CAVS)*, 2019, pp. 1–5.

[6] M. Boban, D. Dupleich, N. Iqbal, J. Luo, C. Schneider, R. Müller, Z. Yu, D. Steer, T. Jämsä, J. Li, and R. S. Thomä, "Multi-band vehicle-to-vehicle channel characterization in the presence of vehicle blockage," *IEEE Access*, vol. 7, pp. 9724–9735, 2019.

[7] D. Dupleich, R. Müller, M. Landmann, E. Shinwasusin, K. Saito, J. Takada, J. Luo, R. Thomä, and G. Del Galdo, "Multi-band propagation and radio channel characterization in street canyon scenarios for 5G and beyond," *IEEE Access*, vol. 7, pp. 160 385–160 396, 2019.

[8] J. Park, J. Lee, K. Kim, M. Kim, and K. C. Lee, "Multipath propagation characteristics for 5G vehicular communications based on 28 GHz expressway measurements," in *2019 13th European Conference on Antennas and Propagation (EuCAP)*, 2019, pp. 1–5.

[9] J. Blumenstein, A. Prokes, J. Vychodil, T. Mikulasek, J. Milos, E. Zöchmann, H. Groll, C. F. Mecklenbräuker, M. Hofer, D. Löschenbrand, L. Bernadó, T. Zemen, S. Sangodoyin, and A. Molisch, "Measured high-resolution power-delay profiles of non-stationary vehicular millimeter wave channels," in *2018 IEEE 29th Annual International Symposium on Personal, Indoor and Mobile Radio Communications (PIMRC)*, 2018, pp. 1–5.

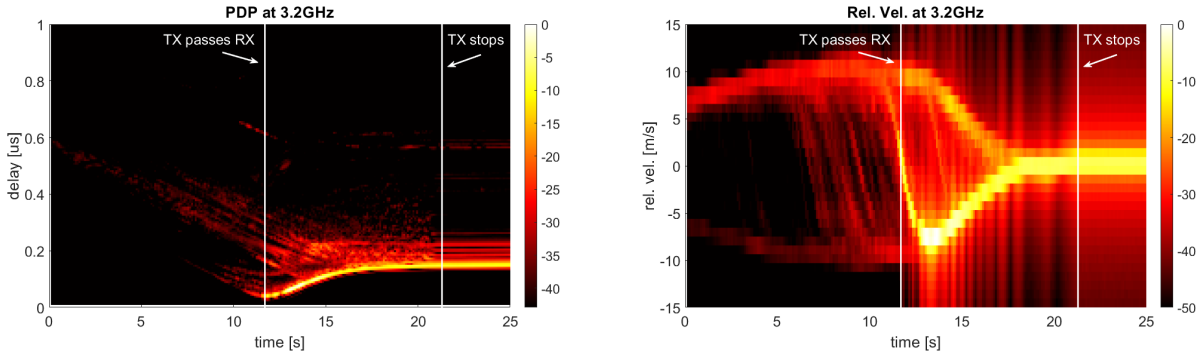

(a) PDP vs. time, max. power normalized to 0 dB.

(b) Rel. vel. vs. time, max. power normalized to 0 dB.

Fig. 7. PDP (left) and DSD (right) for the 3.2 GHz band, Doppler shift axis rescaled to relative velocity.

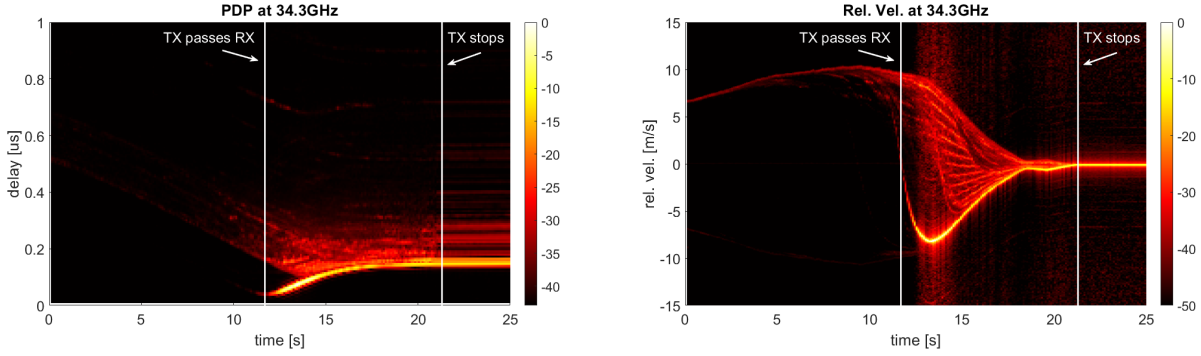

(a) PDP vs. time, max. power normalized to 0 dB.

(b) Rel. vel. vs. time, max. power normalized to 0 dB.

Fig. 8. PDP (left) and DSD (right) for the 34.3 GHz band, Doppler shift axis rescaled to relative velocity.

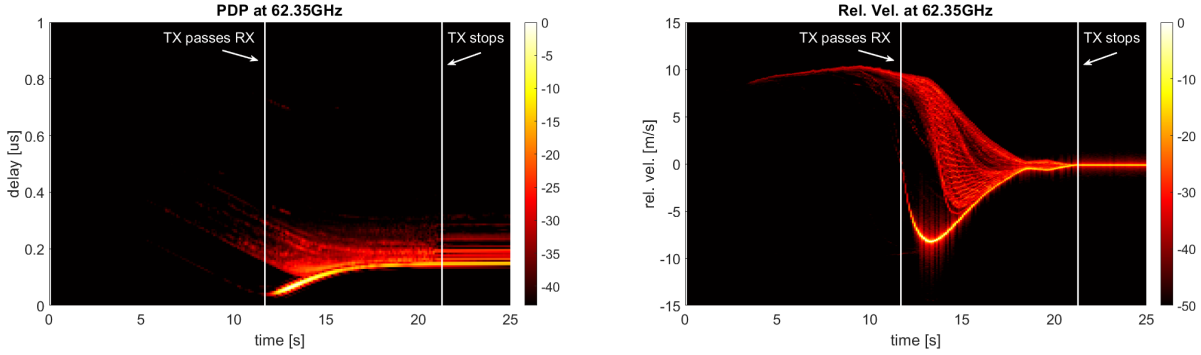

(a) PDP vs. time, max. power normalized to 0 dB.

(b) Rel. vel. vs. time, max. power normalized to 0 dB.

Fig. 9. PDP (left) and DSD (right) for the 62.35 GHz band, Doppler shift axis rescaled to relative velocity.

[10] H. Groll, E. Zöchmann, M. Hofer, H. Hammoud, S. Sangodoyin, T. Zemen, J. Blumenstein, A. Prokes, A. F. Molisch, and C. F. Mecklenbräuker, "60 GHz V2I channel variability for different elevation angle switching strategies," in *2020 14th European Conference on Antennas and Propagation (EuCAP)*, 2020, pp. 1–5.

[11] *Device Specifications, NI USRP-2594R, 10 MHz to 6 GHz Tunable RF Transceiver*, National Instruments.

[12] D. Löschenbrand, M. Hofer, L. Bernadó, G. Humer, B. Schrenk, S. Zelenbaba, and T. Zemen, "Distributed massive MIMO channel measurements in urban vehicular scenario," in *2019 13th European Conference on Antennas and Propagation (EuCAP)*, 2019, pp. 1–5.

[13] S. Zelenbaba, M. Hofer, D. Löschenbrand, G. Kail, M. Schiefer, and T. Zemen, "Spatial properties of industrial wireless ultra-reliable low-latency communication mimo links," in *2019 53rd Asilomar Conference on Signals, Systems, and Computers*, 2019, pp. 1054–1058.

[14] M. Friese, "Multitone signals with low crest factor," *IEEE Transactions on Communications*, vol. 45, no. 10, pp. 1338–1344, 1997.

[15] Stadt Wien - ViennaGIS. [Online]. Available: : www.wien.gv.at/viennagis

[16] L. Bernadó, T. Zemen, F. Tufvesson, A. F. Molisch, and C. F. Mecklenbrauker, "Delay and Doppler spreads of nonstationary vehicular channels for safety-relevant scenarios," *IEEE Trans. Veh. Technol.*, vol. 63, no. 1, pp. 82–93, Jan. 2014.

[17] D. Slepian, "Prolate spheroidal wave functions, Fourier analysis, and uncertainty-V: The discrete case," *Bell Syst. Techn J.*, vol. 57, no. 5, pp. 1371–1430, May 1978.

[18] E. Zöchmann, M. Hofer, M. Lerch, S. Pratschner, L. Bernadó, J. Blumenstein, S. Caban, S. Sangodoyin, H. Groll, T. Zemen, A. Prokeš, M. Rupp, A. F. Molisch, and C. F. Mecklenbräuker, "Position-specific statistics of 60 GHz vehicular channels during overtaking," *IEEE Access*, vol. 7, pp. 14 216–14 232, 2019.